

Frustrated magnets without geometrical frustration in bosonic flux ladders

Luca Barbiero,^{1,*} Josep Cabedo,^{2,*} Maciej Lewenstein,^{3,4} Leticia Tarruell,^{3,4} and Alessio Celi²

¹*Institute for Condensed Matter Physics and Complex Systems,
DISAT, Politecnico di Torino, I-10129 Torino, Italy.*

²*Departament de Física, Universitat Autònoma de Barcelona, E-08193 Bellaterra, Spain[†]*

³*ICFO - Institut de Ciències Fotoniques, The Barcelona Institute of Science and Technology,
Av. Carl Friedrich Gauss 3, 08860 Castelldefels (Barcelona), Spain*

⁴*ICREA, Pg. Lluís Companys 23, 08010 Barcelona, Spain
(Dated: December 13, 2022)*

We propose a scheme to realize the frustrated spin-1/2 quantum XX model with ultracold bosonic atoms in optical lattices. Our approach is based on a square ladder of magnetic flux $\sim \pi$ with one real and one synthetic spin dimension. Although this system does not have geometrical frustration, we show that at low energies it maps into an effective triangular ladder with staggered fluxes for specific values of the synthetic tunneling. We numerically investigate its rich phase diagram and show that it contains bond-ordered-wave and chiral superfluid phases. Our scheme gives access to minimal instances of frustrated magnets *without the need for real geometrical frustration*, in a setup of minimal experimental complexity.

Introduction. The interplay between geometrical frustration and quantum fluctuations leads to exotic states of matter such as resonating valence bond and quantum spin liquid phases [1–3]. The simplest model encompassing the richness of frustrated quantum magnets is the antiferromagnetic Heisenberg Hamiltonian on the triangular lattice [4], which includes deconfined quantum critical points [5–7], anyonic liquids [8], and where spontaneous dimerization and chiral order appear [9–13]. In this work, we focus on a minimal instance of the frustrated antiferromagnetic Heisenberg model, the spin-1/2 quantum XX model on a triangular two-leg ladder. We show that its rich phase diagram can be effectively accessed with ultracold atoms using a semi-synthetic bosonic flux ladder of square lattice geometry, a setup of minimal experimental complexity that is routinely realized with real-space [14, 15] and synthetic dimension approaches [16–24].

While the investigation of spin 1/2 Heisenberg triangular ladder systems in solid state materials is a very active field of research [25–31], the broad tunability of ultracold atoms offers an attractive alternative to investigate magnetic frustration in a pristine setting and gives access to new observables. On the one hand, Fermi gases in triangular optical lattices or optical tweezer arrays provide an ideal implementation of the celebrated $J_1 - J_2$ antiferromagnetic Heisenberg Hamiltonian [32–34], although achieving experimental temperatures below the superexchange energy scale remains a formidable challenge [35, 36]. On the other hand, strongly-interacting bosonic systems subjected to artificial magnetic fluxes also display frustrated magnetic phases, but at the larger (and accessible) energy scale set by the tunneling [37, 38]. However, despite tremendous progress in the realization of artificial gauge fields in such systems using real-space lattices [15, 39–43], the combination of large magnetic fluxes and strong interactions leads to detrimental heat-

ing processes that hinder the investigation of quantum magnetism [44].

An alternative approach, more resilient to heating, is to employ semi-synthetic flux ladders with one fictitious dimension constituted by internal spin states coupled via two-photon Raman transitions [16, 45], a system that has been successfully employed to experimentally investigate few-leg square ladder systems [17–20], but is not straightforward to generalize to triangular geometries without introducing additional heating mechanisms [46, 47]. In this Letter, we propose a scheme to realize a frustrated quantum spin model – inbuilt in a semi-synthetic flux ladder – *without the need for explicit geometrical frustration*. Building on our previous work [48], we show that, when the inter-leg coupling is strong, the square bosonic ladder maps at low energies into an effective triangular system with staggered magnetic fluxes. Related schemes have been very recently proposed in fermionic synthetic ladders [49, 50], although no effective frustration was investigated in this setting. Exploiting our mapping, we identify parameter regimes where geometric frustration plays an important role at accessible temperatures, numerically show that the system displays the same ground state phases as the frustrated spin-1/2 quantum XX model [51], and identify suitable observables to reveal them in current experiments with ultracold atoms.

Model. We consider the two-leg semi-synthetic bosonic flux ladder [16], see Fig. 1(a), described by

$$H_{\square} = \sum_{j,\sigma} \left(-te^{-i\gamma\sigma} a_{j+1,\sigma}^{\dagger} + \frac{\Omega}{4} a_{j,-\sigma}^{\dagger} + \sigma \delta a_{j,\sigma}^{\dagger} \right) a_{j,\sigma} + \text{H.c.} \\ + \sum_{j,\sigma} \left(\frac{U_{\sigma,\sigma}}{2} n_{j,\sigma} (n_{j,\sigma} - 1) + \frac{U_{\sigma,-\sigma}}{2} n_{j,\sigma} n_{j,-\sigma} \right). \quad (1)$$

Here, $a_{i\sigma}^{\dagger} (a_{i\sigma})$ creates (annihilates) a boson in site i of a 1D optical lattice of length L , and two different internal atomic states $\sigma = \pm 1/2$ coupled via two-photon

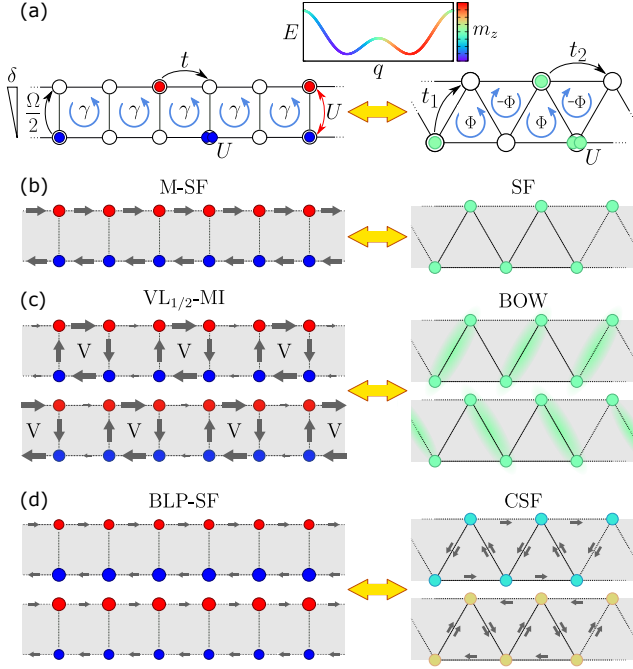


Figure 1. Mapping a semi-synthetic square ladder into a frustrated triangular ladder. (a) Left: original square flux ladder model (1), with intra- and inter-leg tunnelings t and $\Omega/2$, inter-leg offset δ , on- and off-site interactions U , and magnetic flux γ ; Right: truncated lower-band Hamiltonian (2), describing an effective triangular ladder with complex tunnelings t_1 and t_2 , on-site interactions U , and staggered flux Φ . Inset: single-particle dispersion relation of the lower energy band of the square flux ladder for strong Ω and $\gamma \sim \pi$. (b-d) Current (arrow) and density (circle) patterns of the flux ladder phases at average density $\rho = 1/4$ (left), and corresponding phases of the effective triangular model at half-filling (right): (b) Meissner superfluid (M-SF) – superfluid (SF) of the triangular model, (c) vortex lattice insulator ($VL_{1/2}$ -MI) – bond-ordered wave (BOW), and (d) biased-ladder superfluid phase (BLP) – chiral superfluid (CSF). Circles and arrows in the square ladder sketches are scaled according to their numerical values at $\Omega = 10t$ and $\delta = 0$, with γ and U adjusted so that $t_2/|t_1| = 0.2$ in (b), $t_2/|t_1| = 0.5$ in (c) and $t_2/|t_1| = 1.0$ in (d), and $U = 10|t_1|$. Color scale: spin composition m_z of the ground states in the semi-synthetic ladder.

Raman transitions realize the two legs of the ladder. The intra-leg tunneling t is the conventional tunneling rate along the lattice, while the inter-leg tunneling amplitude is proportional to the Raman Rabi frequency Ω . The two-photon Raman detuning yields a potential offset δ between the two legs, and a classical gauge field γ results from the momentum transfer of the Raman beams. Atoms experience intra-leg on-site and inter-leg nearest-neighbor interactions, which we choose identical $U_{\sigma,\sigma} = U_{\sigma,-\sigma} = U$. The total atom number is $N = \sum_{i=1}^L \sum_{\sigma} n_{i,\sigma}$, with $n_{i,\sigma} = a_{i,\sigma}^\dagger a_{i,\sigma}$ the density in site i .

In the strong Raman coupling limit $\Omega \gg t$, the two

single-particle dispersion bands of (1) are well separated by an energy gap $\sim \Omega$ [52]; we denote them lower and higher-band dressed states. When the condition $\Omega \gg U$ is also fulfilled, some of us recently pointed out that the low-energy properties of the system are captured by a Hamiltonian that includes only lower band modes [48]

$$H_\Delta = \sum_{l=1,2} t_l \sum_i (b_i^\dagger b_{i+l} + \text{H.c.}) + \frac{U}{2} \sum_i \tilde{n}_i (\tilde{n}_i - 1), \quad (2)$$

where $b_j^\dagger (b_j)$ are the bosonic creation (annihilation) operators for the inverse-Fourier-transformed lower-band dressed states and $\tilde{n}_j = b_j^\dagger b_j$ (see [52] for the derivation). In this regime, the effective Hamiltonian (2) describes a system of N bosons in a lattice of length L with the same on-site interaction U but with effective nearest neighbor (NN) t_1 and next-nearest neighbor (NNN) t_2 complex tunnelings. It is thus equivalent to a triangular ladder with gauge invariant staggered magnetic flux $\Phi = \pi - 2\delta \tan(\gamma/2)/\Omega + \mathcal{O}[(\delta/\Omega)^2]$, see Fig. 1(a). At $\delta = 0$, the effective tunnelings are real and have opposite signs, and the staggered flux ladder is fully frustrated with $\Phi = \pi$. To order $\mathcal{O}[(t/\Omega)^2]$, the effective tunneling amplitudes in H_Δ relate to the parameters of H_\square by [52]

$$t_1 \simeq -t \cos(\gamma/2) \quad \text{and} \quad t_2 \simeq t^2 \sin^2(\gamma/2)/\Omega. \quad (3)$$

In the ultracold atom context, the triangular Bose-Hubbard ladder Hamiltonian (2) has been mainly studied at unity filling [53–55] and at low densities [56] (for non staggered fluxes see [57]). Moreover, detailed studies of the hardcore boson (HCB) limit ($U \rightarrow \infty$) at half-filling $\tilde{n} = N/L = 1/2$, where the system is further mapped to a frustrated spin-1/2 quantum XX model ($b_i^\dagger, b_j \rightarrow S_i^+, S_j^-$, see [52]) have been performed [51, 58, 59]. In this regime, a gapless superfluid (SF) is found at low values of $|t_2/t_1|$, signaled by the quasi-long range behavior of the single-particle Green's function $g^1(|i-j|) = \langle b_i^\dagger b_j \rangle$. At intermediate values of $|t_2/t_1|$, a gapped translation-breaking bond-ordered-wave (BOW) phase is stabilized, see Fig. 1(c). It is signalled by a nonzero value of the two-point operator $O_{\text{BO}} = \sum_i ((-1)^i/L) (b_i^\dagger b_{i+1} + b_i b_{i+1}^\dagger)$. Moreover, it exhibits a finite charge gap, thus describing an insulating state with $g^1(|i-j|)$ decaying exponentially. Finally, for larger values of $|t_2/t_1|$, a gapless chiral superfluid (CSF) phase emerges. There, the system presents two nonequivalent minima in the dispersion relation, and interatomic interactions favor the occupation of either of the two minima. This yields two degenerate solutions that spontaneously break a Z_2 parity symmetry, see Fig. 1(d), and exhibit a finite chirality $k_i = 2i(b_i b_{i+1}^\dagger - b_i^\dagger b_{i+1})$. The CSF phase can thus be identified by the long-range behavior of the chiral correlation function $k^2(|i-j|) = \langle k_i k_j \rangle$.

In our realization of the triangular model (2), we can widely adjust the ratio $|t_2/t_1|$ while arbitrarily approaching the HCB limit within the effective model by setting

$|t_{1,2}| \ll U \ll \Omega$. Therefore, we expect that at filling $\rho = 1/4$ the whole phase diagram of the quantum XX model can be reproduced in this regime by the flux ladder Hamiltonian (1). There, the three phases described above can be conveniently reinterpreted in terms of the currents and densities of the undressed bosons, which makes them experimentally accessible [52].

The SF phase of the triangular model translates into the Meissner superfluid phase (M-SF) of the flux ladder [60], see 1(b), characterized by vanishing rung currents and off-diagonal quasi-long range order. The BOW phase corresponds to a vortex lattice insulating phase (VL_{1/2}-MI) of maximal vortex filling $\rho_v = 1/2$, where the effective dimers correspond to the vortex plaquettes, see Fig. 1(c). The nature of the BOW phase in the bare basis is easily understood from the susceptibility of the energy against the explicit dimerization of the leg tunnelings [52], through which one can identify

$$O_{\text{BO}} \simeq \sum_{j,\sigma} \frac{2(-1)^j \text{Re}(te^{-i\gamma\sigma} a_{j+1,\sigma}^\dagger a_{j,\sigma})}{Lt \cos(\gamma/2)}. \quad (4)$$

The BOW phase is characterized by the staggered current patterns of the vortices, and is signalled by the staggered leg current

$$j_{sl} = \frac{1}{L} \sum_{j,\sigma} 4\sigma(-1)^j \text{Im} \left(te^{-i\gamma\sigma} a_{j+1,\sigma}^\dagger a_{j,\sigma} \right), \quad (5)$$

together with the exponential decay of the single-particle Green's function. Finally, the CSF corresponds to a biased-ladder superfluid phase (BLP-SF), characterized by a spontaneous density imbalance between the two legs of the ladder [61, 62], see Fig. 1(c). Around $\delta = 0$,

$$k_j \simeq -\frac{2\Omega}{t \sin(\gamma/2)} m_z^{(j)}, \quad (6)$$

where $m_z^{(j)} = \sum_{\sigma} \sigma a_{j,\sigma}^\dagger a_{j,\sigma}$ is the magnetization or the inter-leg population imbalance at site j [52].

Based on these correspondences, we propose to detect the different phases by measuring the response of the system to the explicit breaking of the Z_2 parity and translation symmetries of the Hamiltonian. The former can be easily achieved by setting the Raman detuning δ to a nonzero value. The latter can be implemented by a spatial modulation of the optical lattice using a superlattice potential that dimerizes the lattice structure, parameterized by including in (1) a position dependent tunneling strength $t_j = t(1 + \Delta(-1)^j)$ between sites j and $j+1$. In this way, the spontaneous breaking of the Z_2 symmetry of the ground state in the CSF (or BLP-SF) phase is signaled by the discontinuity in the mean magnetization $m_z = \frac{1}{N} \sum_{i,\sigma} \langle \sigma a_{i,\sigma}^\dagger a_{i,\sigma} \rangle$ around $\delta = 0$. Similarly, the spontaneous dimerization of the BOW (or VL_{1/2}-MI) phase is signalled by the jump of the staggered currents (5) around $\Delta = 0$.

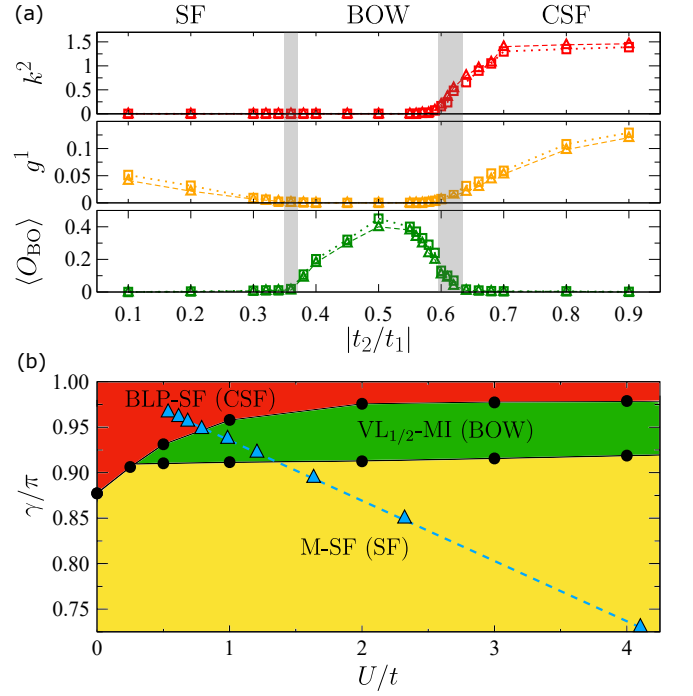


Figure 2. Phase diagram. (a) DMRG-computed values of chiral correlation function k^2 (top panel), single-particle Green's function g^1 (central panel) and two-point bond-order operator O_{BO} (bottom panel) as a function of $|t_2/t_1|$. Triangles: effective triangular staggered flux ladder (2) at half filling, with $U = 10|t_1|$ and $\Phi = \pi$. Squares: square flux ladder (1) at $\rho = 1/4$ and $\delta = 0$, where we have fixed $\Omega = 20t$ and adjusted γ and U to match the corresponding values of t_2/t_1 and $U/|t_1|$. Grey areas: uncertainty on the estimated phase transition points. DMRG simulations use up to 1024 DMRG states and 6 finite-size sweeps. All quantities are extracted via a finite size extrapolation with system lengths up to $L = 120$ ($L = 80$) for the triangular (square) ladder model. (b) Phase diagram of the semi-synthetic square flux ladder (1) at $\rho = 1/4$ for $\Omega = 20t$ and $\delta = 0$. Black circles: phase boundary from DMRG simulations. Blue triangles: set of points where $U = 10t \cos(\gamma/2) = 10|t_1|$ and the effective triangular ladder (2) tunneling ratio $|t_2/t_1|$ takes values from 0.9 to 0.1, corresponding to the curves of (a).

Numerical results. To assess the predictions of the effective model (2), we run density-matrix-renormalization-group (DMRG) [63, 64] simulations of Hamiltonian (1) in the regimes discussed. In Fig. 2(a), we show the values of g^1 , O_{BO} , and k^2 as a function of $|t_1/t_2|$, for the ground states of both the effective triangular Hamiltonian (2) at half-filling (triangles) and the original square ladder Hamiltonian (1) at filling $\rho = 1/4$ (squares). For the latter, we set $\Omega = 20t$, use (3) to retrieve the corresponding values of t_2 and t_1 , and exploit the explicit relations between the dressed (b_n, b_m^\dagger) and bare (a_j, a_k^\dagger) operators, truncated to zero order in (t/Ω) [52], to compute g^1 , O_{BO} , and k^2 . In both cases, the interaction strength is set to $U = 10t \cos(\gamma/2) = 10|t_1|$, which realizes the strongly-interacting regime of the effective

tive triangular ladder. We observe very good agreement between the two models in this regime of parameters. Moreover, the phase diagram predicted in the HCB limit of the effective model [51] is preserved for large but finite values of $U/|t_1|$ and Ω : for sufficiently low $|t_2/t_1|$, a SF (M-SF) phase, uniquely captured by the quasi-long range order of $g^1(|i-j|)$, appears. For higher values of $|t_2/t_1|$ the quasi-long range order is lost and a gapped phase occurs instead. As expected, it is captured by a finite value of O_{BO} , signalling the dimerization that characterizes the BOW phase of the triangular model, or, equivalently, the vortex structures of the $V_{1/2}$ -MI phase in the square ladder (see (4)). Finally, a phase analogous to the CSF of the spin chain appears when $|t_2/t_1|$ is further increased. It is characterized by a finite value of $g^1(|i-j|)$ and the long-range order of $k^2(|i-j|)$, which signal the inter-leg population imbalance of the BLP-SF phase (see (6)).

In Fig. 2(b), we show the phase diagram of the square flux ladder in the $U-\gamma$ plane for $\Omega = 20t$. The blue triangles fix the condition $U = 10t \cos \gamma/2 = 10|t_1|$, and correspond to the curves displayed in Fig. 2(a). Remarkably, the three phases predicted by the effective frustrated XX model persist in wide regions of parameter space. For stronger interactions – where the truncation to the lower band is no longer accurate – a charge density wave phase (not displayed in the figure) has been shown to appear [65, 66], while the M-SF survives to the HCB limit of the flux ladder at quarter filling.

Finally, we numerically assess the protocol described above to probe the three phases in the square flux ladder. Figure 3(a) shows the mean magnetization m_z of the ground state as a function of δ for $\Omega = 10t$. We ad-

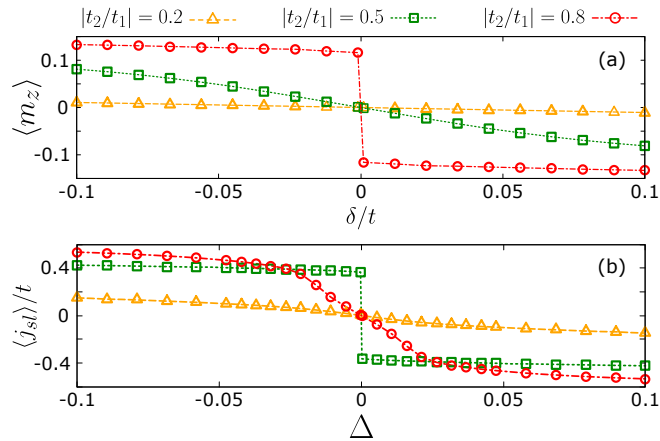


Figure 3. (a) Magnetization m_z as a function of the Raman detuning δ , for the ground state of Hamiltonian (1) at $\rho = 1/4$, with $\Omega = 10t$ and adjusting γ and U so that $U = 10|t_1|$ and $|t_2/t_1| = 0.2$ (red squares), 0.5 (yellow circles), 0.8 (green triangles), with $t_1 < 0$. (b) Staggered leg current j_{sl} defined in (5) as a function of the lattice dimerization Δ . All quantities are extrapolated to the thermodynamic limit by considering system sizes up to $L = 80$.

just γ to different values of $|t_2/t_1|$ and keep $U = 10|t_1|$. For $|t_2/t_1| = 0.8$, the discontinuity in m_z around $\delta = 0$ signals the spontaneous breaking of the Z_2 parity symmetry that characterizes the BLP-SF (CSF) phase. Similarly, Fig. 3(b) shows the expected value of the staggered leg current j_{sl} (see eq.(5)) as a function of Δ . As expected, for $|t_2/t_1| = 0.5$, the spontaneous dimerization that characterizes the $VL_{1/2}$ -MI (BOW) is signalled by the discontinuity of j_{sl} around $\Delta = 0$.

Experimental implementation. The flux ladder model discussed above can be implemented using a Raman-coupled 1D Bose gas subjected to a 1D optical lattice. This approach allows realizing large rung couplings along the synthetic direction with low Raman intensities that ensure small heating rates [18]. For concreteness, we focus on ^{41}K atoms at large magnetic fields, where the low sensitivity of δ to magnetic field fluctuations [67] provides a fine control of the effective staggered flux Φ . However, our scheme can be implemented equivalently with ^{87}Rb atoms using dynamical decoupling schemes [68, 69]. We consider a blue-detuned retro-reflected 1D lattice of wavelength $\lambda_{L,s} = 532$ nm of depth $5E_{L,s}$ for the physics, and an additional retro-reflected lattice of wavelength $\lambda_{L,l} = 1064$ nm overlapped with it for preparing the required $\rho = 1/4$ filling and for dimerizing the system in the symmetry breaking measurements of Fig. 3 [52]. Using two Raman beams at the tune-out wavelength 769 nm and forming a $\sim 45^\circ$ angle with the lattice beams yields the required flux $\gamma \sim \pi$ [16]. In such conditions, the BOW and CSF regimes of the effective triangular model can be realized with tunneling rates $|t_{1,2}|/\hbar$ above 100 Hz, while reaching the strongly interacting regime $U = 10|t_1|$ by confining the gas along the transverse directions with two 1064 nm perpendicular optical lattices of depth $\sim 45E_{L,l}$. Moreover, the Raman coupling $\Omega \sim 10t$ remains sufficiently large to satisfy the lower-band approximation, while enabling gas lifetimes much larger than the tunneling timescales of the effective model [52]. Finally, the magnetization and staggered leg currents of Fig. 3 can be simply determined by measuring the atomic spin populations and staggered leg currents using a combination of Stern-Gerlach, superlattice, and time-of-flight techniques [14, 18]. Thus, our proposal is immediately accessible in current experiments.

Conclusion We have shown that semi-synthetic flux ladders enable the experimental realization of a frustrated XX Heisenberg model with bosons in a lattice without real geometric frustration. Our scheme is robust and does not suffer from the heating limitations of Floquet-engineering or higher bands schemes [39, 40, 70]. Its tunability makes it ideal for detecting multipartite entanglement [71], and for studying transport and out of equilibrium properties, which are challenging for classical numerical simulations but start to be accessible experimentally [24]. Whether such effective low-energy dressed-state descriptions can be successfully applied to

spin models implemented in other experimental platforms [72–79] is an open question worth investigating.

We are grateful to C. S. Chisholm and A. Rubio-Abadal for a critical reading of the manuscript. L. B. acknowledges M. Aidelsburger, N. Baldelli and C. R. Cabrera for discussions on related topics. Research at ICFO was supported by Spanish MCIN/AEI/10.13039/501100011033 Severo Ochoa program for Centres of Excellence in R&D (CEX2019-000910-S) and MCIN Recovery, Transformation and Resilience Plan with funding from European Union NextGenerationEU (PRTR C17.I1), Fundació Privada Cellex, Fundació Mir-Puig, and Generalitat de Catalunya (CERCA program). L. B. acknowledges funding from Politecnico di Torino, starting package Grant No. 54 RSG21BL01. L. B. and M. L. acknowledge funding from European Union (ERC AdG-833801 NOQIA, EU Horizon 2020 FET-OPEN OPTO-Logic (Grant No. 899794), and EU Horizon Europe NeQST (Grant No. 101080086)), Spanish AEI/MCIN/10.13039/501100011033 (FIDEUA PID2019-106901GB-I00, PGC2018-097027-B-I00, and QUSPIN RTC2019-007196-7), EU QUANTERA MAQS (funded by State Research Agency MICN/AEI/10.13039/501100011033, PCI2019-111828-2), Barcelona Supercomputing Center MareNostrum (FI-2022-1-0042), and the Polish National Science Centre (Symfonia Grant No. 2016/20/W/ST4/00314). L. T. acknowledges funding from European Union (ERC CoG-101003295 SuperComp), MCIN/AEI/10.13039/501100011033 (LIGAS PID2020-112687GB-C21), and Deutsche Forschungsgemeinschaft (Research Unit FOR2414, Project No. 277974659). Research at UAB was supported by MCIN/AEI/10.13039/501100011033 (LIGAS PID2020-112687GB-C22). A. C. acknowledges support from the UAB Talent Research program. All authors acknowledge funding from EU QUANTERA DYNAMITE (funded by State Research Agency MICN/AEI/10.13039/501100011033, PCI2022-132919) and from Generalitat de Catalunya (QuantumCAT U16-011424, co-funded by ERDF Operational Program of Catalonia 2014-2020).

* These authors contributed equally to this work.

† Electronic address: josep.cabedo@uab.cat

- [1] P. Anderson, “Resonating valence bonds: A new kind of insulator?” *Mater. Res. Bull.* **8**, 153 (1973).
- [2] L. Balents, “Spin liquids in frustrated magnets,” *Nature* **464**, 199 (2010).
- [3] C. Lacroix, P. Mendels, and F. Mila, *Introduction to Frustrated Magnetism* (Springer-Verlag, Berlin Heidelberg, 2011).
- [4] H. T. Diep, *Frustrated Spin Systems* (World Scientific, Singapore, 2004).
- [5] T. Senthil, A. Vishwanath, L. Balents, S. Sachdev, and M. P. Fisher, “Deconfined quantum critical points,” *Science* **303**, 1490 (2004).
- [6] A. W. Sandvik, “Evidence for deconfined quantum criticality in a two-dimensional Heisenberg model with four-spin interactions,” *Phys. Rev. Lett.* **98**, 227202 (2007).
- [7] S. Jiang and O. Motrunich, “Ising ferromagnet to valence bond solid transition in a one-dimensional spin chain: Analogies to deconfined quantum critical points,” *Phys. Rev. B* **99**, 075103 (2019).
- [8] A. Rahmani, A. E. Feiguin, and C. D. Batista, “Anyonic liquids in nearly saturated spin chains,” *Phys. Rev. Lett.* **113**, 267201 (2014).
- [9] C. Majumdar and D. Ghosh, “On next-nearest-neighbor interaction in linear chain. I,” *J. Math. Phys.* **10**, 1388 (1969).
- [10] F. D. M. Haldane, “Spontaneous dimerization in the $S = \frac{1}{2}$ Heisenberg antiferromagnetic chain with competing interactions,” *Phys. Rev. B* **25**, 4925 (1982).
- [11] K. Okamoto and K. Nomura, “Fluid-dimer critical point in $S = 1/2$ antiferromagnetic Heisenberg chain with next nearest neighbor interactions,” *Phys. Lett. A* **169**, 433 (1992).
- [12] S. R. White and I. Affleck, “Dimerization and incommensurate spiral spin correlations in the zigzag spin chain: Analogies to the Kondo lattice,” *Phys. Rev. B* **54**, 9862 (1996).
- [13] A. A. Nersesyan, A. O. Gogolin, and F. H. L. Eßler, “Incommensurate spin correlations in spin-1/2 frustrated two-leg Heisenberg ladders,” *Phys. Rev. Lett.* **81**, 910 (1998).
- [14] M. Atala, M. Aidelsburger, M. Lohse, J. T. Barreiro, B. Paredes, and I. Bloch, “Observation of chiral currents with ultracold atoms in bosonic ladders,” *Nat. Phys.* **10**, 588 (2014).
- [15] M. E. Tai, A. Lukin, M. Rispoli, R. Schittko, T. Menke, D. Borgnia, P. M. Preiss, F. Grusdt, A. M. Kaufman, and M. Greiner, “Microscopy of the interacting Harper-Hofstadter model in the two-body limit,” *Nature* **546**, 519 (2017).
- [16] A. Celi, P. Massignan, J. Ruseckas, N. Goldman, I. Spielman, G. Juzeliūnas, and M. Lewenstein, “Synthetic gauge fields in synthetic dimensions,” *Phys. Rev. Lett.* **112**, 043001 (2014).
- [17] M. Mancini, G. Pagano, G. Cappellini, L. Livi, M. Rider, J. Catani, C. Sias, P. Zoller, M. Inguscio, M. Dalmonte, and L. Fallani, “Observation of chiral edge states with neutral fermions in synthetic Hall ribbons,” *Science* **349**, 1510 (2015).
- [18] B. K. Stuhl, H.-I. Lu, L. M. Ayccock, D. Genkina, and I. B. Spielman, “Visualizing edge states with an atomic Bose gas in the quantum Hall regime,” *Science* **349**, 1514 (2015).
- [19] L. F. Livi, G. Cappellini, M. Diem, L. Franchi, C. Clivati, M. Frittelli, F. Levi, D. Calonico, J. Catani, M. Inguscio, and L. Fallani, “Synthetic dimensions and spin-orbit coupling with an optical clock transition,” *Phys. Rev. Lett.* **117**, 220401 (2016).
- [20] S. Kolkowitz, S. L. Bromley, T. Bothwell, M. L. Wall, G. E. Marti, A. Koller, X. Zhang, A. M. Rey, and J. Ye, “Spin-orbit-coupled fermions in an optical lattice clock,” *Nature* **542**, 66 (2017).

- [21] J. H. Han, J. H. Kang, and Y. Shin, “*Band gap closing in a synthetic Hall tube of neutral fermions*,” *Phys. Rev. Lett.* **122**, 065303 (2019).
- [22] C.-H. Li, Y. Yan, S.-W. Feng, S. Choudhury, D. B. Blasing, Q. Zhou, and Y. P. Chen, “*Bose-Einstein condensate on a synthetic topological Hall cylinder*,” *PRX Quantum* **3**, 010316 (2022).
- [23] R. P. Anderson, D. Trypogeorgos, A. Valdés-Curiel, Q.-Y. Liang, J. Tao, M. Zhao, T. Andrijauskas, G. Juzeliūnas, and I. B. Spielman, “*Realization of a deeply subwavelength adiabatic optical lattice*,” *Phys. Rev. Res.* **2**, 013149 (2020).
- [24] T. W. Zhou, G. Cappellini, D. Tusi, L. Franchi, J. Paravicini, C. Repellin, S. Greschner, M. Inguscio, T. Giamarchi, M. Filippone, J. Catani, and L. Fallani, “*Observation of universal Hall response in strongly interacting fermions*,” arXiv:2205.13567.
- [25] S.-L. Drechsler, O. Volkova, A. N. Vasiliev, N. Tristan, J. Richter, M. Schmitt, H. Rosner, J. Málek, R. Klingeler, A. A. Zvyagin, and B. Büchner, “*Frustrated cuprate route from antiferromagnetic to ferromagnetic spin- $\frac{1}{2}$ Heisenberg chains: $\text{Li}_2\text{ZrCuO}_4$ as a missing link near the quantum critical point*,” *Phys. Rev. Lett.* **98**, 077202 (2007).
- [26] C. de Graaf, I. de P. R. Moreira, F. Illas, O. Iglesias, and A. Labarta, “*Magnetic structure of Li_2CuO_2 : from ab initio calculations to macroscopic simulations*,” *Phys. Rev. B* **66**, 014448 (2002).
- [27] A. U. B. Wolter, F. Lipps, M. Schäpers, S.-L. Drechsler, S. Nishimoto, R. Vogel, V. Kataev, B. Büchner, H. Rosner, M. Schmitt, M. Uhlarz, Y. Skourski, J. Wosnitza, S. Süllow, and K. C. Rule, “*Magnetic properties and exchange integrals of the frustrated chain cuprate $\text{PbCuSO}_4(\text{OH})_2$* ,” *Phys. Rev. B* **85**, 014407 (2012).
- [28] H.-J. Grafe, S. Nishimoto, M. Iakovleva, E. Vavilova, L. Spillecke, A. Alfonsov, M.-I. Sturza, S. Wurmehl, H. Nojiri, H. Rosner, J. Richter, U. K. Rößler, S.-L. Drechsler, V. Kataev, and B. Büchner, “*Signatures of a magnetic field-induced unconventional nematic liquid in the frustrated and anisotropic spin-chain cuprate LiCuSbO_4* ,” *Sci Rep* **7**, 6720 (2017).
- [29] A. Orlova, E. L. Green, J. M. Law, D. I. Gorbunov, G. Chanda, S. Krämer, M. Horvatić, R. K. Kremer, J. Wosnitza, and G. L. J. A. Rikken, “*Nuclear magnetic resonance signature of the spin-nematic phase in LiCuVO_4 at high magnetic fields*,” *Phys. Rev. Lett.* **118**, 247201 (2017).
- [30] H. Ueda, S. Onoda, Y. Yamaguchi, T. Kimura, D. Yoshizawa, T. Morioka, M. Hagiwara, M. Hagihala, M. Soda, T. Masuda, T. Sakakibara, K. Tomiyasu, S. Ohira-Kawamura, K. Nakajima, R. Kajimoto, M. Nakamura, Y. Inamura, N. Reynolds, M. Frontzek, J. S. White, M. Hase, and Y. Yasui, “*Emergent spin-1 Haldane gap and ferroelectricity in a frustrated spin- $\frac{1}{2}$ ladder*,” *Phys. Rev. B* **101**, 140408 (2020).
- [31] C. P. Grams, D. Brünig, S. Kopatz, T. Lorenz, P. Becker, L. Bohatý, and J. Hemberger, “*Observation of chiral solitons in LiCuVO_4* ,” *Commun. Phys.* **5**, 37 (2022).
- [32] L. Tarruell, D. Greif, T. Uehlinger, G. Jotzu, and T. Esslinger, “*Creating, moving and merging Dirac points with a Fermi gas in a tunable honeycomb lattice*,” *Nature* **483**, 302 (2012).
- [33] J. Yang, L. Liu, J. Mongkolkeha, and P. Schauss, “*Site-resolved imaging of ultracold fermions in a triangular-lattice quantum gas microscope*,” *PRX Quantum* **2**, 020344 (2021).
- [34] Z. Z. Yan, B. M. Spar, M. L. Prichard, S. Chi, H.-T. Wei, E. Ibarra-García-Padilla, K. R. A. Hazzard, and W. S. Bakr, “*A two-dimensional programmable tweezer array of fermions*,” arXiv:2203.15023.
- [35] A. Mazurenko, C. S. Chiu, G. Ji, M. F. Parsons, M. Kanász-Nagy, R. Schmidt, F. Grusdt, E. Demler, D. Greif, and M. Greiner, “*A cold-atom Fermi-Hubbard antiferromagnet*,” *Nature* **545**, 462 (2017).
- [36] J. Mongkolkeha, L. Liu, D. Garwood, J. Yang, and P. Schauss, “*Quantum gas microscopy of a geometrically frustrated Hubbard system*,” arXiv:2210.14895.
- [37] A. Eckardt, P. Hauke, P. Soltan-Panahi, C. Becker, K. Sengstock, and M. Lewenstein, “*Frustrated quantum antiferromagnetism with ultracold bosons in a triangular lattice*,” *EPL* **89**, 10010 (2010).
- [38] A. Celi, T. Grass, A. J. Ferris, B. Padhi, D. Raventós, J. Simonet, K. Sengstock, and M. Lewenstein, “*Modified spin-wave theory and spin-liquid behavior of cold bosons on an inhomogeneous triangular lattice*,” *Phys. Rev. B* **94**, 075110 (2016).
- [39] J. Struck, C. Ölschläger, R. Le Targat, P. Soltan-Panahi, A. Eckardt, M. Lewenstein, P. Windpassinger, and K. Sengstock, “*Quantum simulation of frustrated classical magnetism in triangular optical lattices*,” *Science* **333**, 996 (2011).
- [40] J. Struck, M. Weinberg, C. Ölschläger, P. Windpassinger, J. Simonet, K. Sengstock, R. Höppner, P. Hauke, A. Eckardt, M. Lewenstein, and L. Mathey, “*Engineering Ising-XY spin-models in a triangular lattice using tunable artificial gauge fields*,” *Nat. Phys.* **9**, 738 (2013).
- [41] M. Aidelsburger, M. Atala, S. Nascimbène, S. Trotzky, Y.-A. Chen, and I. Bloch, “*Experimental realization of strong effective magnetic fields in an optical lattice*,” *Phys. Rev. Lett.* **107**, 255301 (2011).
- [42] M. Aidelsburger, M. Atala, M. Lohse, J. T. Barreiro, B. Paredes, and I. Bloch, “*Realization of the Hofstadter Hamiltonian with ultracold atoms in optical lattices*,” *Phys. Rev. Lett.* **111**, 185301 (2013).
- [43] H. Miyake, G. A. Siviloglou, C. J. Kennedy, W. C. Burton, and W. Ketterle, “*Realizing the Harper Hamiltonian with laser-assisted tunneling in optical lattices*,” *Phys. Rev. Lett.* **111**, 185302 (2013).
- [44] C. Weitenberg and J. Simonet, “*Tailoring quantum gases by Floquet engineering*,” *Nat. Phys.* **17**, 1342 (2021).
- [45] O. Boada, A. Celi, J. I. Latorre, and M. Lewenstein, “*Quantum simulation of an extra dimension*,” *Phys. Rev. Lett.* **108**, 133001 (2012).
- [46] E. Anisimovas, M. Račiūnas, C. Sträter, A. Eckardt, I. B. Spielman, and G. Juzeliūnas, “*Semisynthetic zigzag optical lattice for ultracold bosons*,” *Phys. Rev. A* **94**, 063632 (2016).
- [47] D. Suszalski and J. Zakrzewski, “*Different lattice geometries with a synthetic dimension*,” *Phys. Rev. A* **94**, 033602 (2016).
- [48] J. Cabedo, J. Claramunt, J. Mompart, V. Ahufinger, and A. Celi, “*Effective triangular ladders with staggered flux from spin-orbit coupling in 1d optical lattices*,” *Eur. Phys. J. D* **74**, 1 (2020).

- [49] M. Mamaev, I. Kimchi, R. M. Nandkishore, and A. M. Rey, “Tunable-spin-model generation with spin-orbit-coupled fermions in optical lattices,” *Phys. Rev. Res.* **3**, 013178 (2021).
- [50] M. Mamaev, T. Bilitewski, B. Sundar, and A. M. Rey, “Resonant Dynamics of Strongly Interacting $SU(n)$ Fermionic Atoms in a Synthetic Flux Ladder,” *PRX Quantum* **3**, 030328 (2022).
- [51] M. Sato, S. Furukawa, S. Onoda, and A. Furusaki, “Competing phases in spin-1/2 $J_1 - J_2$ chain with easy-plane anisotropy,” *Mod. Phys. Lett. B* **25**, 901 (2011).
- [52] See Supplemental Material, which also includes refs. [80–84] for details.
- [53] S. Greschner, L. Santos, and T. Vekua, “Ultracold bosons in zig-zag optical lattices,” *Phys. Rev. A* **87**, 033609 (2013).
- [54] M. P. Zaletel, S. A. Parameswaran, A. Rüegg, and E. Altman, “Chiral bosonic Mott insulator on the frustrated triangular lattice,” *Phys. Rev. B* **89**, 155142 (2014).
- [55] C. Romen and A. M. Läuchli, “Chiral Mott insulators in frustrated Bose-Hubbard models on ladders and two-dimensional lattices: A combined perturbative and density matrix renormalization group study,” *Phys. Rev. B* **98**, 054519 (2018).
- [56] S. Greschner and T. Mishra, “Interacting bosons in generalized zigzag and railroad-trestle models,” *Phys. Rev. B* **100**, 144405 (2019).
- [57] C.-M. Halati and T. Giamarchi, “Bose-Hubbard triangular ladder in an artificial gauge field,” *arXiv:2210.14594*.
- [58] T. Mishra, R. V. Pai, S. Mukerjee, and A. Paramekanti, “Quantum phases and phase transitions of frustrated hard-core bosons on a triangular ladder,” *Phys. Rev. B* **87**, 174504 (2013).
- [59] T. Mishra, R. V. Pai, and S. Mukerjee, “Supersolid in a one-dimensional model of hard-core bosons,” *Phys. Rev. A* **89**, 013615 (2014).
- [60] E. Orignac and T. Giamarchi, “Meissner effect in a bosonic ladder,” *Phys. Rev. B* **64**, 144515 (2001).
- [61] R. Wei and E. J. Mueller, “Theory of bosons in two-leg ladders with large magnetic fields,” *Phys. Rev. A* **89**, 063617 (2014).
- [62] A. Tokuno and A. Georges, “Ground states of a Bose-Hubbard ladder in an artificial magnetic field: field-theoretical approach,” *New J. Phys.* **16**, 073005 (2014).
- [63] S. R. White, “Density matrix formulation for quantum renormalization groups,” *Phys. Rev. Lett.* **69**, 2863 (1992).
- [64] M. Fishman, S. R. White, and E. M. Stoudenmire, “The ITensor Software Library for Tensor Network Calculations,” *arXiv:2007.14822*.
- [65] M. Piraud, F. Heidrich-Meisner, I. P. McCulloch, S. Greschner, T. Vekua, and U. Schollwöck, “Vortex and Meissner phases of strongly interacting bosons on a two-leg ladder,” *Phys. Rev. B* **91**, 140406 (2015).
- [66] S. Greschner, M. Piraud, F. Heidrich-Meisner, I. P. McCulloch, U. Schollwöck, and T. Vekua, “Symmetry-broken states in a system of interacting bosons on a two-leg ladder with a uniform abelian gauge field,” *Phys. Rev. A* **94**, 063628 (2016).
- [67] M. Buser, C. Hubig, U. Schollwöck, L. Tarruell, and F. Heidrich-Meisner, “Interacting bosonic flux ladders with a synthetic dimension: Ground-state phases and quantum quench dynamics,” *Phys. Rev. A* **102**, 053314 (2020).
- [68] D. Trypogeorgos, A. Valdés-Curiel, N. Lundblad, and I. B. Spielman, “Synthetic clock transitions via continuous dynamical decoupling,” *Phys. Rev. A* **97**, 013407 (2018).
- [69] R. P. Anderson, M. J. Kewming, and L. D. Turner, “Continuously observing a dynamically decoupled spin-1 quantum gas,” *Phys. Rev. A* **97**, 013408 (2018).
- [70] X.-Q. Wang, G.-Q. Luo, J.-Y. Liu, G.-H. Huang, Z.-X. Li, C. Wu, A. Hemmerich, and Z.-F. Xu, “Observation of nematic orbital superfluidity in a triangular optical lattice,” *arXiv:2211.05578*.
- [71] S. Singha Roy, L. Carl, and P. Hauke, “Genuine multipartite entanglement in a one-dimensional Bose-Hubbard model with frustrated hopping,” *Phys. Rev. B* **106**, 195158 (2022).
- [72] S. de Léséleuc, V. Lienhard, P. Scholl, D. Barredo, S. Weber, N. Lang, H. P. Büchler, T. Lahaye, and A. Browaeys, “Observation of a symmetry-protected topological phase of interacting bosons with Rydberg atoms,” *Science* **365**, 775 (2019).
- [73] V. Lienhard, P. Scholl, S. Weber, D. Barredo, S. de Léséleuc, R. Bai, N. Lang, M. Fleischhauer, H. P. Büchler, T. Lahaye, and A. Browaeys, “Realization of a density-dependent Peierls phase in a synthetic, spin-orbit coupled Rydberg system,” *Phys. Rev. X* **10**, 021031 (2020).
- [74] T. Graß, C. Muschik, A. Celi, R. W. Chhajlany, and M. Lewenstein, “Synthetic magnetic fluxes and topological order in one-dimensional spin systems,” *Phys. Rev. A* **91**, 063612 (2015).
- [75] Y. Shapira, T. Manovitz, N. Akerman, A. Stern, and R. Ozeri, “Quantum simulations of interacting systems with broken time-reversal symmetry,” *arXiv:2205.11178v1*.
- [76] A. V. Gorshkov, S. R. Manmana, G. Chen, J. Ye, E. Demler, M. D. Lukin, and A. M. Rey, “Tunable superfluidity and quantum magnetism with ultracold polar molecules,” *Phys. Rev. Lett.* **107**, 115301 (2011).
- [77] J. L. Bohn, A. M. Rey, and J. Ye, “Cold molecules: Progress in quantum engineering of chemistry and quantum matter,” *Science* **357**, 1002 (2017).
- [78] J. S. Douglas, H. Habibian, C.-L. Hung, A. V. Gorshkov, H. J. Kimble, and D. E. Chang, “Quantum many-body models with cold atoms coupled to photonic crystals,” *Nat. Photon.* **9**, 326 (2015).
- [79] D. E. Chang, J. S. Douglas, A. González-Tudela, C.-L. Hung, and H. J. Kimble, “Colloquium: Quantum matter built from nanoscopic lattices of atoms and photons,” *Rev. Mod. Phys.* **90**, 031002 (2018).
- [80] C. K. Majumdar, “Antiferromagnetic model with known ground state,” *J. Phys. C: Solid State Phys.* **3**, 911 (1970).
- [81] S. Greschner, M. Piraud, F. Heidrich-Meisner, I. P. McCulloch, U. Schollwöck, and T. Vekua, “Spontaneous increase of magnetic flux and chiral-current reversal in bosonic ladders: Swimming against the tide,” *Phys. Rev. Lett.* **115**, 190402 (2015).
- [82] A. Frölian, “Simulating a topological gauge theory in a Raman-dressed Bose-Einstein condensate” (Ph.D. thesis, Universitat Politècnica de Catalunya, 2022).
- [83] R. Wei and E. J. Mueller, “Magnetic-field dependence of raman coupling in alkali-metal atoms,” *Phys. Rev. A* **87**, 042514 (2013).

- [84] A. Frölian, C. S. Chisholm, E. Neri, C. R. Cabrera, R. Ramos, A. Celi, and L. Tarruell, “*Realizing a 1D topological gauge theory in an optically dressed BEC,*” Nature **608**, 293 (2022).

Supplemental Material

In this Supplemental Material we include the detailed derivation of the lower-band Hamiltonian (2) presented in the main text. Furthermore, we discuss the nature of the symmetry-broken phases of the effective model back in the original undressed basis, and discuss the meaningful observables of the effective frustrated model in terms of the original square flux ladder. Finally, we briefly assess the experimental viability of our proposal.

DRESSED BASIS EFFECTIVE TRIANGULAR LADDER

In the absence of inter-atomic interactions, Hamiltonian (1) in the main text is block diagonal in orthogonal quasimomentum subspaces, $H_{\text{kin}} = \sum_q H_q$, with

$$H_q = \left(2t \sin\left(\frac{\gamma}{2}\right) \sin(q) + \frac{\delta}{2} \right) \sigma_z - 2t \cos\left(\frac{\gamma}{2}\right) \cos(q) + \frac{\Omega}{2} \sigma_x. \quad (\text{S1})$$

Here, σ_j are the spin-1/2 Pauli matrices, which act on the pseudospin space spanned by the coupled pair of internal states. In the diagonal or dressed basis, the noninteracting Hamiltonian can be rewritten as

$$H_{\text{kin}} = \sum_{q,m=\pm} \epsilon_{q,m} \tilde{b}_{q,m}^\dagger \tilde{b}_{q,m}, \quad (\text{S2})$$

where the two dispersion bands are given by

$$\epsilon_{q,\pm} = \pm \frac{\Omega}{2} \sqrt{1 + (\tilde{q} + \tilde{\delta})^2} - 2t \cos\left(\frac{\gamma}{2}\right) \cos(q), \quad (\text{S3})$$

and where

$$\tilde{b}_{q,m'}^\dagger = \sum_m U_{m',m}(q) \tilde{a}_{q,m}^\dagger, \quad (\text{S4})$$

are the dressed modes of the noninteracting system. Here, we define $\tilde{q} \equiv \frac{4t \sin(\gamma/2) \sin(q)}{\Omega}$ and $\tilde{\delta} \equiv \delta/\Omega$, and $U = e^{i\sigma_y \theta_q/2}$ is the unitary transformation that relates the bare and the dressed basis, with $\cos(\theta_q) = \frac{\tilde{q} + \tilde{\delta}}{\sqrt{1 + (\tilde{q} + \tilde{\delta})^2}}$, $0 \leq \theta_q \leq \pi$.

We now consider the regime where the rung tunneling Ω (the Raman coupling strength) is the dominant energy scale, and the two dispersion bands are well separated. We can then safely neglect the highest-band dressed states and truncate Hamiltonian (S2) to

$$H_{\text{kin}} = \sum_q \epsilon_{q,-} \tilde{b}_{q,-}^\dagger \tilde{b}_{q,-}. \quad (\text{S5})$$

Finally, we introduce the inverse-Fourier-transformed truncated basis, the dressed modes

$$b_n^\dagger \equiv \frac{1}{\sqrt{L}} \sum_q e^{-iqn} \tilde{b}_{q,-}^\dagger = \frac{1}{L} \sum_{m,q,n'} e^{iq(n'-n)} U_{-,m}(q) a_{n',m}^\dagger, \quad (\text{S6})$$

and substitute (S6) into (S5), which yields

$$H_{\text{kin}} \simeq \sum_n \sum_l t_l b_{n+l}^\dagger b_n, \quad (\text{S7})$$

with

$$t_l = \frac{1}{L} \sum_q e^{-iq l} \epsilon_{q,-}. \quad (\text{S8})$$

By rewriting U explicitly in terms of \tilde{q} and $\tilde{\delta}$, and considering the regime where $\tilde{q} \ll 1$, we have

$$U_{-, \pm} = \pm \frac{1}{\sqrt{2}} \sqrt{1 \pm \frac{\tilde{q} + \tilde{\delta}}{\sqrt{1 + (\tilde{q} + \tilde{\delta})^2}}} = \pm \frac{1}{\sqrt{2}} \sqrt{1 \pm \frac{\tilde{\delta}}{\sqrt{1 + \tilde{\delta}^2}}} + \frac{\tilde{q}}{2\sqrt{2}(1 + \tilde{\delta}^2)^{3/2} \sqrt{1 \pm \frac{\tilde{\delta}}{\sqrt{1 + \tilde{\delta}^2}}}} + O(\tilde{q}^2). \quad (\text{S9})$$

By introducing (S9) into (S6) and taking the limit $L \rightarrow \infty$, we obtain the following expression for the dressed mode operators b_j^\dagger in the bare basis $a_{j,m}^\dagger$

$$b_j^\dagger = \frac{1}{\sqrt{2}} \sqrt{1 + \frac{\tilde{\delta}}{\sqrt{1 + \tilde{\delta}^2}}} a_{j,+}^\dagger - \frac{1}{\sqrt{2}} \sqrt{1 - \frac{\tilde{\delta}}{\sqrt{1 + \tilde{\delta}^2}}} a_{j,-}^\dagger + i \frac{t \sin(\gamma/2)}{\sqrt{2}\Omega(1 + \tilde{\delta}^2)^{3/2}} \left(\frac{a_{j+1,+}^\dagger - a_{j-1,+}^\dagger}{\sqrt{1 - \frac{\tilde{\delta}}{\sqrt{1 + \tilde{\delta}^2}}}} + \frac{a_{j+1,-}^\dagger - a_{j-1,-}^\dagger}{\sqrt{1 + \frac{\tilde{\delta}}{\sqrt{1 + \tilde{\delta}^2}}}} \right) + O((t/\Omega)^2). \quad (\text{S10})$$

Similarly, we can expand the expression for the effective tunneling coefficients t_l . From

$$\epsilon_{q,-} = -\frac{\Omega}{2} \left(\sqrt{1 + \tilde{\delta}^2} + \frac{\tilde{\delta}\tilde{q}}{\sqrt{1 + \tilde{\delta}^2}} + \frac{\tilde{q}^2}{2(1 + \tilde{\delta}^2)^{3/2}} + O(\tilde{q}^3) \right) - 2t \cos(\gamma/2) \cos(q), \quad (\text{S11})$$

and taking the limit $L \rightarrow \infty$, it follows that

$$t_l = -t \left[\left(\frac{\Omega}{2t} \sqrt{1 + (\delta/\Omega)^2} + \frac{2t \sin^2(\gamma/2)}{\Omega(1 + (\delta/\Omega)^2)^{3/2}} \right) \delta_{l,0} + \left(\cos(\gamma/2) \mp i \frac{\delta \sin(\gamma/2)}{\Omega \sqrt{1 + (\delta/\Omega)^2}} \right) \delta_{l,\pm 1} - \frac{t \sin^2(\gamma/2)}{\Omega(1 + \delta^2/\Omega^2)^{3/2}} \delta_{l,\pm 2} + O((t/\Omega)^2) \right]. \quad (\text{S12})$$

In this way, to first order in t/Ω , the dressed Hamiltonian (S7) can be written as

$$H_{\text{kin}} = \sum_i (t_1 b_{i+1}^\dagger b_i + t_2 b_{i+2}^\dagger b_i + \text{H.c.}) = - \sum_i (|t_1| e^{i\phi_1} b_{i+1}^\dagger b_i + |t_2| e^{i\phi_2} b_{i+2}^\dagger b_i + \text{H.c.}), \quad (\text{S13})$$

where we drop the constant term $t_0 N$ and only nearest and next-nearest neighbor couplings are kept. Hamiltonian (S13) is equivalent to a triangular ladder with gauge invariant staggered flux $\Phi = \phi_2 - 2\phi_1$, with $\phi_1 = \arg(-t_1)$ and $\phi_2 = \arg(-t_2)$. Remarkably, in the chosen gauge the NN tunneling coefficient t_1 has a nonzero imaginary contribution that is linearly proportional to the Raman detuning δ , see (S12). To first order in δ/Ω , we then have

$$\phi_1 = -\frac{\delta \tan(\gamma/2)}{\Omega}, \quad \phi_2 = \pi. \quad (\text{S14})$$

Hence, at linear order in δ/Ω around $\delta = 0$, we can tune the staggered flux Φ while leaving $|t_1|$ and $|t_2|$ unchanged. By setting $\delta = 0$, the ladder is fully frustrated, with $|\Phi| = \pi$, and we recover the expressions in (3) from the main text.

Finally, if the interaction energy per particle is much smaller than the band gap, given by

$$\Delta\epsilon = \min(\epsilon_{q,+} - \epsilon_{q,-}) = \Omega \left(1 - 4 \cos(\gamma/2) \frac{t}{\Omega} + O((t + \delta)^2/\Omega^2) \right), \quad (\text{S15})$$

inter-atomic interactions can be treated within the lower band truncation. We consider SU(2) symmetric interactions

$$H_{\text{int}} = \frac{U}{2} \sum_n N_n (N_n - 1), \quad (\text{S16})$$

where $N_n = \sum_m a_{n,m}^\dagger a_{n,m}$. After truncating the expressions of $a_{n,m}$ and $a_{n,m}^\dagger$ to the lower band states, one has

$$N_n \simeq \sum_{l,l'} C_{l,l'} b_{n+l}^\dagger b_{n+l'}, \quad (\text{S17})$$

with

$$C_{l,l'} = \frac{1}{L^2} \sum_{q,q'} e^{i(ql - q'l')} \sum_m U_{-,m}(q) U_{-,m}^*(q'). \quad (\text{S18})$$

From eqs. (S9) and (S16) to (S18), it follows that

$$H_{\text{int}} \simeq \frac{U}{2} \sum_n b_n^\dagger b_n (b_n^\dagger b_n - 1) + O((t/\Omega)^2). \quad (\text{S19})$$

By combining the kinetic and interaction parts of the Hamiltonian (S19) and (S13), and truncating to first order in t/Ω , we recover the expression of the complete effective Hamiltonian (2) from the main text, which describes a triangular ladder configuration with tunable on-site interactions, tunnelings, and staggered flux, and is schematically represented in Fig. 1(a) of the main text.

The effective bosonic ladder can be further mapped to an XX frustrated spin chain by considering hard-core bosons, with $U/|t_{1,2}| \rightarrow \infty$ and thus rendering double occupancies energetically forbidden. One can then identify $(b_i^\dagger, b_j) \rightarrow (S_i^+, S_j^-)$, which leads to

$$H_\Delta \xrightarrow{U/t_1 \rightarrow \infty} \sum_j (t_1 S_j^- S_{j+1}^+ + t_2 S_j^- S_{j+2}^+ + \text{H.c.}). \quad (\text{S20})$$

If we set $\delta = 0$, or equivalently the effective staggered flux $\Phi = \pi$, such a HCB Hamiltonian describes a t_1 - t_2 spin- $\frac{1}{2}$ XX -chain

$$H_\Delta(\Phi = \pi) \xrightarrow{U/t_1 \rightarrow \infty} 2t_1 \sum_j (S_j^x S_{j+1}^x + S_j^y S_{j+1}^y) + 2t_2 \sum_j (S_j^x S_{j+2}^x + S_j^y S_{j+2}^y), \quad (\text{S21})$$

from which we infer the presence of frustrated regimes in the original semi-synthetic square flux ladder.

CURRENT AND DENSITY STRUCTURES OF THE SYMMETRY-BROKEN PHASES

BOW phase as a vortex lattice insulator

To gain insights on the nature of the BOW insulating phase of the effective triangular model back in the original square ladder, we now look at the properties of the ground state in the parameter regime that corresponds to the so-called Majumdar-Ghosh point of the XX spin model (S21), that is, at $t_2 = -t_1/2 > 0$ and $t_1/U \rightarrow 0$. There, the system is exactly solvable [80], with the ground state of the Hamiltonian being two-fold degenerate in the thermodynamic limit. Each solution spontaneously breaks the lattice translation symmetry of (S21) and have periodicity two. Both are given by dimerized product states of triplet spin states defined on pairs of consecutive sites

$$|\psi_{e,o}\rangle = \bigotimes_{j \in \text{even/odd}} \frac{|\uparrow_j \downarrow_{j+1}\rangle + |\downarrow_j \uparrow_{j+1}\rangle}{\sqrt{2}} = \prod_{j \in \text{even/odd}} \frac{b_j^\dagger + b_{j+1}^\dagger}{\sqrt{2}} |0\rangle. \quad (\text{S22})$$

Without loss of generality, in the following derivation we use $|\psi_e\rangle$. The ground state $|\psi_e\rangle$ can be written as

$$|\psi_e\rangle = \prod_{j=0}^{L-1} D_j^\dagger |0\rangle, \quad (\text{S23})$$

where we have defined the operators

$$D_j^\dagger = \frac{b_{2j}^\dagger + b_{2j+1}^\dagger}{\sqrt{2}}, \quad (\text{S24})$$

which fulfill $[D_j, D_k^\dagger] = \delta_{j,k}$. At $\delta = 0$, we conveniently reexpress the dressed mode operators (S6), truncated to first order in t/Ω , as

$$b_n^\dagger \simeq \cos \alpha c_{n,-}^\dagger + i \sin \alpha \frac{c_{n+1,+}^\dagger - c_{n-1,+}^\dagger}{\sqrt{2}}, \quad (\text{S25})$$

where we have defined $c_{n,\pm}^\dagger = \frac{a_{n,+}^\dagger \pm a_{n,-}^\dagger}{\sqrt{2}}$ and $\alpha = \arctan\left(\frac{\sqrt{2}t \sin(\gamma/2)}{\Omega}\right)$. By substituting the approximate expression (S25) for the modes b_j into (S24), we can write D_j in the bare basis $\{c_{j,m}^\dagger |0\rangle\}$ as

$$D_j^\dagger \simeq \cos \alpha \frac{c_{2j,-}^\dagger + c_{2j+1,-}^\dagger}{\sqrt{2}} + i \sin \alpha \frac{c_{2j+2,+}^\dagger + c_{2j+1,+}^\dagger - c_{2j,+}^\dagger - c_{2j-1,+}^\dagger}{2}. \quad (\text{S26})$$

We now compute the vortex currents in the paired sites. We start by computing the expected value of the total rung current in the $2k$ plaquette, $j_{2k}^{(r)}$, defined as

$$\begin{aligned} j_{2k}^{(r)} &= i\Omega \left(a_{2k,+} a_{2k,-}^\dagger - a_{2k,+}^\dagger a_{2k,-} \right) - i\Omega \left(a_{2k+1,+} a_{2k+1,-}^\dagger - a_{2k+1,+}^\dagger a_{2k+1,-} \right) \\ &= -i\Omega \left(c_{2k,+} c_{2k,-}^\dagger - c_{2k,+}^\dagger c_{2k,-} \right) + i\Omega \left(c_{2k+1,+} c_{2k+1,-}^\dagger - c_{2k+1,+}^\dagger c_{2k+1,-} \right). \end{aligned}$$

By using expression (S23) and the commutation relations of operators D_j , it is easy to show that

$$\begin{aligned} \langle \psi_e | j_{2k}^{(r)} | \psi_e \rangle &= \langle 0 | D_{k-1} D_k D_{k+1} j_{2k}^{(r)} D_{k-1}^\dagger D_k^\dagger D_{k+1}^\dagger | 0 \rangle \\ &= \langle 0 | D_{k-1} D_k D_{k+1} \left[j_{2k}^{(r)}, D_{k-1}^\dagger \right] D_k^\dagger D_{k+1}^\dagger | 0 \rangle \\ &\quad + \langle 0 | D_{k-1} D_k D_{k+1} D_{k-1}^\dagger \left[j_{2k}^{(r)}, D_k^\dagger \right] D_{k+1}^\dagger | 0 \rangle \\ &\quad + \langle 0 | D_{k-1} D_k D_{k+1} D_{k-1}^\dagger D_k^\dagger \left[j_{2k}^{(r)}, D_{k+1}^\dagger \right] | 0 \rangle. \end{aligned} \quad (\text{S27})$$

Finally, inserting (S26) into eq. (S27) and (S31) yields

$$\langle \psi_e | j_{2k}^{(r)} | \psi_e \rangle = -\frac{\Omega}{\sqrt{2}} \sin \alpha \cos \alpha = -t \sin(\gamma/2) + O((t/\Omega)^3). \quad (\text{S28})$$

Similarly, we now compute the leg currents

$$j_k^\pm = it \left(e^{\mp i\gamma/2} a_{k,\pm} a_{k+1,\pm}^\dagger - e^{\pm i\gamma/2} a_{k,\pm}^\dagger a_{k+1,\pm} \right). \quad (\text{S29})$$

In the $c_{j,m}^\dagger$ basis, the total leg current in the $2k$ plaquette reads

$$\begin{aligned} j_k^{(a)} \equiv j_k^- - j_k^+ &= -t \left(c_{k,+} c_{k+1,+}^\dagger + c_{k,-} c_{k+1,-}^\dagger \right) \sin(\gamma/2) \\ &\quad - it \left(c_{k,+} c_{k+1,-}^\dagger + c_{k,-} c_{k+1,+}^\dagger \right) \cos(\gamma/2) + \text{H.c.} \end{aligned} \quad (\text{S30})$$

Again, we can write

$$\begin{aligned} \langle \psi_e | j_{2k}^{(a)} | \psi_e \rangle &= \langle 0 | D_{k-1} D_k D_{k+1} j_{2k}^{(a)} D_{k-1}^\dagger D_k^\dagger D_{k+1}^\dagger | 0 \rangle \\ &= \langle 0 | D_{k-1} D_k D_{k+1} \left[j_{2k}^{(a)}, D_{k-1}^\dagger \right] D_k^\dagger D_{k+1}^\dagger | 0 \rangle \\ &\quad + \langle 0 | D_{k-1} D_k D_{k+1} D_{k-1}^\dagger \left[j_{2k}^{(a)}, D_k^\dagger \right] D_{k+1}^\dagger | 0 \rangle \\ &\quad + \langle 0 | D_{k-1} D_k D_{k+1} D_{k-1}^\dagger D_k^\dagger \left[j_{2k}^{(a)}, D_{k+1}^\dagger \right] | 0 \rangle. \end{aligned} \quad (\text{S31})$$

which after inserting (S26) results in

$$\begin{aligned} \langle \psi_e | j_{2k}^{(a)} | \psi_e \rangle &= -t \cos(\gamma/2) \sqrt{2} \sin \alpha \cos \alpha - t \sin(\gamma/2) \left(\cos^2 \alpha - \frac{1}{2} \sin^2 \alpha \right) \\ &= -t \sin(\gamma/2) \left(1 + \frac{2t \cos(\gamma/2)}{\Omega} + O((t/\Omega)^2) \right). \end{aligned} \quad (\text{S32})$$

To zero order in (t/Ω) , we have $j_{2k}^{(a)} = j_{2k}^{(r)}$. This result can be extended to the $|\psi_o\rangle$ solution by just shifting each lattice site from j to $j+1$. Therefore, the ground state solutions at the solvable Majumdar-Ghosh point correspond,

in the original square ladder at quarter filling, to two vortex lattice states with vortex filling $\rho_v = 1/2$. The vortex current $j_j^{(c)} = j_j^{(a)} + j_j^{(r)}$ on the dimerized plaquettes is given by

$$\langle \psi_e | j_{2k}^{(c)} | \psi_e \rangle = \langle \psi_o | j_{2k+1}^{(c)} | \psi_o \rangle = -2t \sin(\gamma/2) + O(t/\Omega). \quad (\text{S33})$$

The first order correction to these solutions includes a small current $\propto t \cos(\gamma/2)/\Omega$ between the dimerized plaquettes that vanishes both for $t/\Omega \rightarrow 0$ and $\gamma \rightarrow \pi$. Notice that both solutions have a nonzero chiral current

$$j_c = it \frac{2}{L} \sum_i \sum_{\sigma=\pm 1/2} \sigma (e^{-i\gamma\sigma} a_{i+1,\sigma}^\dagger a_{i,\sigma} - e^{i\gamma\sigma} a_{i+1,\sigma} a_{i,\sigma}^\dagger). \quad (\text{S34})$$

In particular, we have

$$\langle \psi_{e,o} | j_c | \psi_{e,o} \rangle = t \sin(\gamma/2)/2 + O(t/\Omega). \quad (\text{S35})$$

This net edge current is induced by the static gauge field that breaks the time-reversal symmetry in Hamiltonian (1) from the main text. These results have been derived assuming a HCB limit within the effective model, thus, to zero order in t/U , and to first order in t/Ω . As we verified numerically, corrections to this leading behavior are tiny in the range of parameters considered in this work, where $U \gg |t_1|$ and $\Omega \gg t$, and a good qualitative agreement persists even for significantly smaller Ω . The current distribution in the BOW state is schematically represented in Fig. 1(b) from the main text, both in the effective model and in the semi-synthetic flux ladder model. For the latter, we set $\Omega = 10t$, $\delta = 0$ and $\gamma = 0.877\pi$, for which $t_2/|t_1| \sim 0.5$. The arrows representing the currents are scaled according to the values found numerically via DMRG simulations. The insulating nature of such a vortex phase can be inferred from the properties of the BOW phase of the XX model, which is confirmed by numerical simulations of the full ladder model. Indeed, DMRG simulations reveal the exponential decay of the one-body correlator g^1 with the total length of the ladder (see main text and Fig. 2a), and also a finite single-particle excitation gap and a vanishing central charge when the system is extrapolated to the thermodynamic limit. In this way, we can identify the BOW phase of the lowest-band model with a vortex lattice insulating phase of vortex filling $\rho_v = 1/2$ (VL_{1/2}-MI) back in the original square flux ladder.

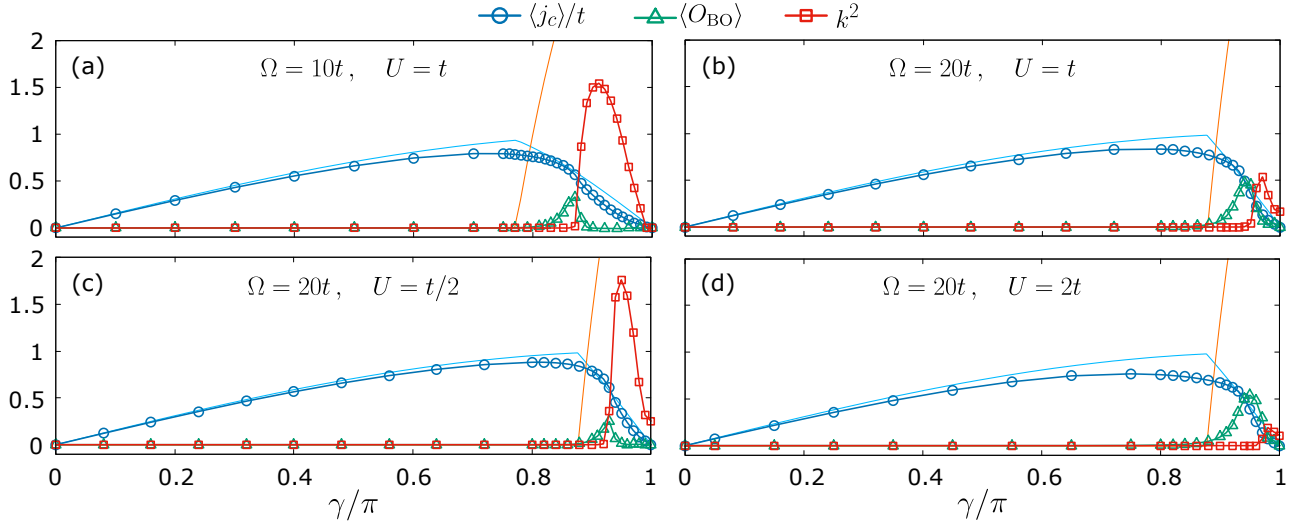


Figure S1. Expected value of the chiral current j_c (blue circles), the bond-order operator O_{BO} (green triangles) and the triangular ladder chiral correlation function $k^2(L)$ (red squares) as a function of γ for the ground state of Hamiltonian (1) in the main text at $\rho = 1/4$. We set $\Omega = 10t$ and $U = t$ in (a), $\Omega = 20t$ and $U = t$ in (b), $\Omega = 20t$ and $U = 0.5t$ in (c), and $\Omega = 20t$ and $U = 2t$ in (d). Cyan and orange thin solid lines show the expected values of the chiral current and chiral correlation functions, respectively, in the noninteracting limit. Without interactions, no BOW exists and the bond-order operator O_{BO} is identically zero, as indicated by the light-green thin solid line. In all cases, the values are obtained from a finite size extrapolation considering sizes up to $L = 80$.

The CSF as a biased ladder superfluid

Similarly, the CSF phase of the effective triangular model has two degenerate solutions that spontaneously break the Z_2 parity symmetry of the Hamiltonian (2), which corresponds to the spin-inversion symmetry, i.e. parity in the synthetic dimension, in the semi-synthetic square ladder, in addition to the $U(1)$ phase symmetry. In each solution, local interatomic interactions favor the occupation of quasimomentum states around either the left or the right minimum of the band. In the corresponding regimes of semi-synthetic flux ladder, the same behavior is expected. The current and density structure of the analogous phase back in the square ladder model is straightforwardly understood by taking the noninteracting limit of the two solutions $|\psi_{L,R}\rangle$, which are then simply given by the collective occupation of the band states located the left and right band minima, respectively.

The single-particle band modes all have a vanishing rung current. For a bandstate at q , it follows

$$\begin{aligned} \langle 0 | \tilde{b}_{q,-} j_k^{(r)} \tilde{b}_{q,-}^\dagger | 0 \rangle &= \frac{i\Omega}{2L} \sum_{nn'mm'} \langle 0 | e^{-iqn'} e^{iqn} U_{-,m'}^*(q) U_{-,m}(q) a_{n',m'} a_{k,-} a_{k,+}^\dagger a_{n,m}^\dagger | 0 \rangle + \text{H.c.} \\ &= -\frac{\Omega}{L} \text{Im} (U_{-,-}^*(q) U_{-,+}(q)) = 0. \end{aligned} \quad (\text{S36})$$

The leg current is given by

$$\begin{aligned} \langle 0 | \tilde{b}_{q,-} j_k^\pm \tilde{b}_{q,-}^\dagger | 0 \rangle &= \frac{it}{L} \sum_{nn'mm'} \langle 0 | e^{\mp i\gamma/2} e^{-iqn'} e^{iqn} U_{-,m'}^*(q) U_{-,m}(q) a_{n',m'} a_{k,\pm} a_{k+1,\pm}^\dagger a_{n,m}^\dagger | 0 \rangle \\ &\quad + \text{H.c.} \\ &= -\frac{2}{L} \text{Im} \left(t e^{-i(q \pm \gamma/2)} U_{-, \pm}^*(q) U_{-, \pm}(q) \right) = \frac{2t}{L} \sin(q \pm \gamma/2) |U_{-, \pm}(q)|^2, \end{aligned} \quad (\text{S37})$$

which yields a nonzero edge current

$$\langle 0 | \tilde{b}_{q,-} j_c \tilde{b}_{q,-}^\dagger | 0 \rangle = \frac{2t}{L} \sin(q + \gamma/2) |U_{-,+}(q)|^2 - \frac{2t}{L} \sin(q - \gamma/2) |U_{-,-}(q)|^2. \quad (\text{S38})$$

At the same time, the band modes have a spin composition that depends on quasimomentum

$$\langle m_z \rangle = \langle 0 | \tilde{b}_{q,-} \frac{n_{q,+} - n_{q,-}}{2} \tilde{b}_{q,-}^\dagger | 0 \rangle = |U_{-,+}(q)|^2 - |U_{-,-}(q)|^2. \quad (\text{S39})$$

If we now set $\delta = 0$, where $U_{-, \pm}(q) = \frac{1}{\sqrt{2}} (1 \pm t \sin(\gamma/2) \sin(q)/\Omega) + O(\tilde{q}^2)$, see eq. (S9), we have

$$\langle j_c \rangle = \frac{2t}{L} \left(\sin(\gamma/2) \cos(q) + \frac{2t}{\Omega} \sin(\gamma) \sin(q)^2 + O((t/\Omega)^2) \right), \quad (\text{S40})$$

and

$$\langle m_z \rangle = \frac{2t \sin(\gamma/2)}{\Omega} \sin(q) + O((t\Omega)^2). \quad (\text{S41})$$

For $|\gamma| < |\gamma_c| = \left| 4 \tan^{-1} \left(\sqrt{\frac{\sqrt{(\Omega/t)^2 + 8^2} - 8}{\Omega/t}} \right) \right|$, the lower band exhibits a single minimum at $q_m = 0$, and the solutions correspond to the noninteracting limit of the Meissner phase: indeed, in this regime the chiral current increases with γ as $\langle j_c \rangle \propto \sin(\gamma/2)$, effectively screening the applied flux. Likewise, the solutions have a vanishing magnetization, that is, they evenly populate the two legs of the ladder.

For $|\gamma| > \gamma_c$, the band splits into two degenerate minima at $q_{R,L} = \pm \cos^{-1} \left(\frac{\Omega \sqrt{1 + (4t \sin(\gamma/2)/\Omega)^2}}{4t \tan(\gamma/2)} \right)$, and the chiral current for the corresponding states $|\psi_{R,L}\rangle$ starts to decrease with an increasing flux γ . In the absence of interactions, the change is nonanalytical in the thermodynamic limit, signalling a second order phase transition. This decrease in the flux screening is shared by the vortex superfluid phase of the flux ladder. However, in the CSF phase predicted by the effective model, the spontaneous occupation of either one of the two band minima $q_{R,L}$ prevents the formation of vortices. Instead, it gives rise to a population imbalance between the two legs, with $\langle m_z \rangle^{R,L} = \frac{2t \sin(\gamma/2)}{\Omega} \sin(q_{L,R})$. The CSF phase, thus, corresponds to a biased-ladder superfluid (BLP-SF) phase [61, 62, 66, 81] back in the square

flux ladder (see below). The currents and densities distributions in the CSF regime are schematically represented in Fig. 1(c) from the main text.

The presence of interatomic interactions smooths out the single-minima to two-minima transition by favoring a spread of the momentum distribution that carries over into the two minima regime of the single-particle energy band. At particle filling $\rho = 1/4$ and in the presence of interatomic interactions, the Meissner to BLP transition is eventually lost in favor of the additional vortex lattice insulator phase in-between, that corresponds to the BOW dimer phase in the effective triangular model. Figure Fig. S1 shows the expected values of the chiral current $\langle j_c \rangle$, O_{BO} and $k^2(L)$ for the ground state at $\rho = 1/4$ as a function of γ for different values of U and Ω . The light-colored blue and orange solid thin lines show the corresponding values obtained for the noninteracting flux ladder. At large γ , nonzero values of $O_{\text{BO}}(L)$ and $k^2(L)$ for $L \rightarrow \infty$ signal the onset of the BOW and CSF phases, respectively. The BOW phase is favored at larger Ω and U . Contrarily, the CSF phase is suppressed by increasing atom-atom interactions and rung tunneling strengths. Still, the phase is expected to persist at fluxes $\gamma \sim \pi$ even for $\Omega \gg t$ and $U \gg |t_1|, t_2$, as is predicted by the HCB limit of the lower-band model.

MEASURING THE OBSERVABLES OF THE EFFECTIVE MODEL

The effective chirality as inter-leg population imbalance

By using equation (S14), we can rewrite the effective chirality k_j in terms of the susceptibility of the Hamiltonian against the interleg energy imbalance δ . As shown in the previous sections, the parameters of the effective triangular model depend on δ only through the NN tunneling phase term ϕ_1 , with $|t_1|$ and t_2 being constant to the order of approximation (see (S12) and (S14)). With this in mind, it is easy to see that the effect of adding small local perturbations to δ simply results in a small spatial modulation of ϕ_1 , and we can write

$$\phi_1^{(j)} = -\frac{\delta_j \tan(\gamma/2)}{\Omega}, \quad (\text{S42})$$

where $\delta_j \sim \delta$ is the interleg energy imbalance at site j . In turn, since we have $\text{Im}(t_1) = 0 + O(\delta/\Omega)$ (see (S12)), in the vicinity of $\delta = 0$ we can approximate $\text{Im}(t_1 b_{j+1}^\dagger b_j) \simeq t_1 \text{Im}(b_{j+1}^\dagger b_j)$, and write the chirality k_j as

$$k_j = 4 \text{Im}(b_{j+1}^\dagger b_j) \simeq \frac{1}{t_1} 4 \text{Im}(t_1 b_{j+1}^\dagger b_j) = -\frac{2}{t_1} \frac{\partial H_\Delta}{\partial \phi_1^{(j)}} \Big|_{|t_1|, \phi_1^{(k)}, t_2}, \quad (\text{S43})$$

with $k \neq j$. From (S43) and (S42), and given that $H_\square \simeq H_\Delta$ in the regimes considered, it follows that

$$k_j \approx \frac{2}{t_1} \frac{\partial \delta_j}{\partial \phi_1} \Big|_{|t_1|, \phi_1^{(k)}, t_2} \frac{\partial H_\square}{\partial \delta_j} \Big|_{|t_1|, \phi_1^{(k)}, t_2} = -\frac{2\Omega}{t \sin(\gamma/2)} \frac{\partial H_\square}{\partial \delta_j} \Big|_{|t_1|, \phi_1^{(k)}, t_2} \quad (\text{S44})$$

Note that since $\phi_1^{(k \neq j)}$, $|t_1|$ and t_2 are independent of δ_j at linear order, we have

$$\frac{\partial H_\square}{\partial \delta_j} \Big|_{|t_1|, \phi_1^{(k)}, t_2} = \frac{\partial H_\square}{\partial \delta_j} \Big|_{\Omega, \gamma, \delta_k} = \frac{\partial H_\square}{\partial \delta_j} \Big|_{\Omega, \gamma, \delta_k} = \sum_{\sigma} \sigma a_{j,\sigma}^\dagger a_{j,\sigma}, \quad (\text{S45})$$

and thus the chirality can be calculated over the original model with

$$k_j \approx -\frac{2\Omega}{t \sin(\gamma/2)} m_z^{(j)}, \quad (\text{S46})$$

where we have defined the local magnetization as

$$m_z^{(j)} = \sum_{\sigma} \sigma a_{i,\sigma}^\dagger a_{i,\sigma}. \quad (\text{S47})$$

Measuring the dimerization of the ground state

The BOW phase is characterized by the spontaneous dimerization of the ground state, with two degenerate solutions that spontaneously break the translation symmetry of the Hamiltonian. Similarly, we can characterize the phase by

the behavior of the system against the explicit breaking of the symmetry. Let us introduce an additional parameter Δ to the Hamiltonian

$$H_{\square}(\Delta) = \sum_{j,\sigma=\pm 1/2} \left(-t(1 + \Delta(-1)^j) e^{-i\gamma\sigma} a_{j+1,\sigma}^{\dagger} + \frac{\Omega}{4} a_{j,-\sigma}^{\dagger} + \sigma \delta a_{j,\sigma}^{\dagger} \right) a_{j,\sigma} + \text{H.c.} \\ + \sum_{j,\sigma} \left(\frac{U_{\sigma,\sigma}}{2} n_{j\sigma}(n_{j\sigma} - 1) + \frac{U_{\sigma,-\sigma}}{2} n_{j,\sigma} n_{j-\sigma} \right). \quad (\text{S48})$$

Here, Δ fixes a relative dimerization of the longitudinal (spatial) tunneling in the square ladder. To first order, the addition of an infinitesimal value of Δ results into a dimerization of the effective triangular ladder

$$H_{\Delta}(\Delta) \simeq \sum_j (t_1(1 + \Delta(-1)^j) b_j^{\dagger} b_{j+1} + t_2 b_j^{\dagger} b_{j+2} + \text{H.c.}) + \frac{U}{2} \sum_i \tilde{n}_i(\tilde{n}_i - 1), \quad (\text{S49})$$

that allows us to write the O_{BO} observable in the original basis as

$$O_{\text{BO}} = \frac{1}{Lt_1} \frac{\partial H_{\Delta}}{\partial \Delta} \simeq -\frac{1}{Lt \cos(\gamma/2)} \frac{\partial H_{\square}}{\partial \Delta} = \frac{1}{Lt \cos(\gamma/2)} \sum_{j,\sigma} (-1)^j 2 \text{Re} \left(t e^{-i\gamma\sigma} a_{j+1,\sigma}^{\dagger} a_{j,\sigma} \right). \quad (\text{S50})$$

Furthermore, in the BOW phase the dimers in the effective triangular ladder correspond to vortices in the square ladder. With this in mind, it can be experimentally more convenient to probe the dimerization of the system simply by measuring the staggered current patterns. For instance, by measuring the response of the current

$$j_{sl} = \frac{1}{L} \sum_{j,\sigma} (-1)^j 4\sigma \text{Im} \left(t e^{-i\gamma\sigma} a_{j+1,\sigma}^{\dagger} a_{j,\sigma} \right) \quad (\text{S51})$$

against the variation of Δ around $\Delta = 0$, the BOW ($\text{VL}_{1/2}$ -MI) phase can be distinguished from the SF (M-SF) and CSF (BLP-SF) phases, as discussed in the main text. Similarly, one could equivalently measure the staggered pattern of the rung currents instead.

EXPERIMENTAL CONSIDERATIONS

Atomic species. The semi-synthetic bosonic flux ladder discussed in the main text can be implemented with essentially any optically-coupled bosonic atomic species, including Raman-coupled ^{87}Rb . In this work, we focus instead on ^{41}K because the energy splitting of states $|\uparrow\rangle \equiv |F=1, m_F=-1\rangle$ and $|\downarrow\rangle \equiv |F=1, m_F=0\rangle$ at a magnetic field $B_0 = 338.4$ G is to first order insensitive to magnetic field fluctuations, allowing for an excellent control of the two-photon Raman detuning δ [82] to which the BOW phase is quite sensitive, see Fig. S2. Moreover, at B_0 the scattering lengths characterizing the interatomic interactions have an almost perfect $\text{SU}(2)$ character ($a_{\uparrow\uparrow} = 60.9a_0$, $a_{\downarrow\downarrow} = 61a_0$, and $a_{\uparrow\downarrow} = 60.7a_0$), as assumed in the main text.

1D optical lattice. To realize the real-space dimension of the semi-synthetic ladder, the atoms must be subjected to a 1D optical lattice. We select a short lattice wavelength $\lambda_{L,s} = 532$ nm and a retro-reflected beam configuration in order to minimize the lattice spacing $d_s = \lambda_{L,s}/2$, since this enhances the lattice recoil energy $E_{L,s} = \hbar^2/(8md_s^2)$ and thus the characteristic energy scales of the effective model (see below). Here \hbar is Planck's constant and m the mass of ^{41}K . For a lattice depth $V_{L,s} = 5E_{L,s}$, the tunneling rate in the square ladder configuration is $t/\hbar \simeq 1.1$ kHz. Moreover, the atoms need to be tightly confined along the transverse directions to enter the one-dimensional regime. This can be achieved using two additional retro-reflected optical lattices along the perpendicular directions with wavelength $\lambda_{L,l} = 1064$ nm and depth $V_{L,l} \sim 46E_{L,l}$, which will create an array of decoupled one-dimensional lattice systems. In these conditions, the interaction energy becomes $U/\hbar \sim 2.1$ kHz and its value can be finely controlled by adjusting the transverse confinement.

Raman coupling. The tunneling along the synthetic dimension is provided by coupling states $|\uparrow\rangle$ and $|\downarrow\rangle$ via two-photon Raman transitions with Rabi coupling strength Ω , which provide easy access to the regime $\Omega = 10t$. We select the potassium tune-out value $\lambda_R = 769$ nm for the Raman beams. This ensures a favorable ratio of the Rabi coupling to the inelastic photon scattering rate by spontaneous emission from the Raman beams – which leads to heating – and does not create an additional scalar potential on the atoms. To obtain a synthetic flux $\gamma \sim \pi$, each of the Raman beams must form an angle $\theta_R \sim 45^\circ$ with the lattice beams, since $\gamma/(2\pi) = (\lambda_{L,s}/\lambda_R) \cos \theta_R$ [16]. The exact flux value can be adjusted by controlling θ_R (see below).

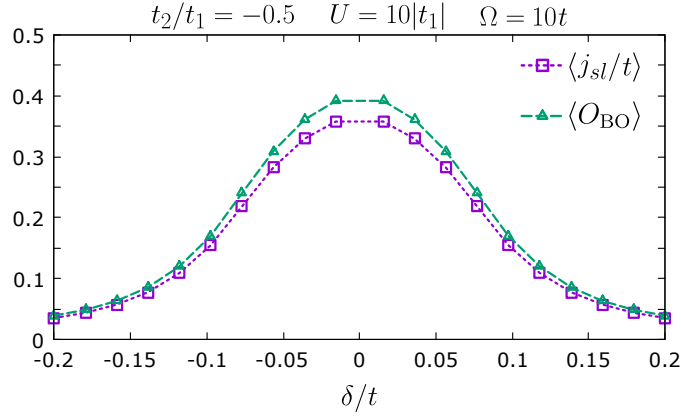


Figure S2. Expected value of staggered leg current j_{sl} (purple square dots, see eq.(S51)) and O_{BO} (green triangle dots) of the ground state of Hamiltonian (1) in the main text as a function of δ , with $\Omega = 10t$ and γ and U adjusted so that $U = 10|t_1|$ and $t_2/|t_1| = 0.5$. All quantities are extrapolated to the thermodynamic limit by considering system sizes up to $L = 80$.

State preparation with an optical superlattice. The phases investigated in this work appear at half-filling in the effective triangular lattice, which corresponds to quarter filling in the original square flux ladder. Disregarding the synthetic spin dimension, the required filling in the original 1D lattice is therefore $1/2$ particle per site. To obtain this value, a robust strategy consists on preparing first a unity-filled Mott insulator in a $\lambda_{L,l} = 1064$ nm retro-reflected lattice, where the lattice spacing is twice d_s , before transferring the atoms to the final $\lambda_{L,s} = 532$ nm lattice. This will result in a half-filled 1D lattice and, after turning on the synthetic Raman tunneling, yield the required $\rho = 1/4$ filling in the synthetic square flux ladder.

Experimental scales. The BOW phase appears in the strongly-interacting regime of the effective model. Realizing it requires both a large band gap and a small bandwidth, and thus large values of Ω . Specifically, setting as above $t/h = 1.1$ kHz and $\Omega = 10t$, the tunneling in the effective model becomes $|t_1/h| \sim 213$ Hz and the corresponding interaction energy $U/h \sim 2.1$ kHz (which remains unchanged) corresponds to $U/|t_1| \sim 10$. To access the BOW regime, i.e. $|t_2/t_1| \sim 1/2$, a flux $\gamma \sim 0.88\pi$ is then required, which can be obtained by setting the an angle of the Raman beams with respect to the lattice beams to $\theta_R \sim 50.5^\circ$. Finally, for $\Omega = 10t$ the inelastic photon scattering from the Raman beams due to spontaneous emission we expect a gas lifetime of about 140 ms [83, 84], which is about 30 times larger than the characteristic tunneling timescales of the effective model.

Detection. The symmetry breaking measurements of Fig. 3 of the main text are straightforward to implement experimentally. On the one hand, the magnetization vs. detuning curve can be simply determined by measuring the leg populations – which in a semi-synthetic ladder correspond to the spin populations – through Stern-Gerlach separation in a time-of-flight experiment. On the other hand, for the staggered leg current vs. lattice dimerization curve, the dimerizing potential can be obtained using the same 1064 nm optical superlattice as for the preparation scheme, and the staggered leg current can be determined from the plaquette dynamics as in previous experiments [14]. Thus, our proposal should be immediately accessible to current experiments.